Valley-dependent band structure and valley polarization in periodically modulated graphene

Wei-Tao Lu*

School of Science and Institute of Condensed Matter Physics, Linyi University, 276005 Linyi, China

(Received 3 April 2016; revised manuscript received 30 June 2016; published 2 August 2016)

The valley-dependent energy band and transport property of graphene under a periodic magnetic-strained field are studied, where the time-reversal symmetry is broken and the valley degeneracy is lifted. The considered superlattice is composed of two different barriers, providing more degrees of freedom for engineering the electronic structure. The electrons near the K and K' valleys are dominated by different effective superlattices. It is found that the energy bands for both valleys are symmetric with respect to $k_y = -(A_M + \xi A_S)/4$ under the symmetric superlattices. More finite-energy Dirac points, more prominent collimation behavior, and new crossing points are found for K' valley. The degenerate miniband near the K valley splits into two subminibands and produces a new band gap under the asymmetric superlattices. The velocity for the K' valley is greatly renormalized compared with the K valley, and so we can achieve a finite velocity for the K valley while the velocity for the K' valley is zero. Especially, the miniband and band gap could be manipulated independently, leading to an increase of the conductance. The characteristics of the band structure are reflected in the transmission spectra. The Dirac points and the crossing points appear as pronounced peaks in transmission. A remarkable valley polarization is obtained which is robust to the disorder and can be controlled by the strain, the period, and the voltage.

DOI: 10.1103/PhysRevB.94.085403

I. INTRODUCTION

Graphene is the most exciting material in condensed matter today, which has inspired people to search for other two-dimensional Dirac materials [1], such as silicene and germanene, in the same group. In pristine graphene, the valence and conduction bands touch at two degenerate but inequivalent valleys at the corner of the Brillouin zone. The two valleys K and K' are related by the time-reversal symmetry. The linear spectrum and the chiral nature give rise to abundant new physics and potential applications in nanoelectronic devices. However, a technological challenge in application is the absence of band gap [2]. Therefore, several methods have been proposed to modify the band structure and control the transport of graphene, such as nanoribbons [3–5], substrate strains [6–9], and magnetic fields [10–13].

One significant feature of graphene is the valley degree of freedom, which can be used to store and process information, referred to as valleytronics. Valleytronics aims to generate and manipulate a valley-polarized current. In the pioneering work by Beenakker *et al.* [14,15], the valley filter and valley valve effect have been proposed in graphene nanoribbons with a zigzag edge, originating from intervalley scattering by a potential step. Subsequently, several improved approaches to realize the valley filter were reported by utilizing the trigonal warping effect of the energy dispersion [16,17], topological line defects [18–21], and electrostatic gates in bilayer graphene [22]. After the discovery of the strain-induced pseudomagnetic fields which could lead to a shift of the K and K' valleys in the opposite direction [23], the high polarization of the valley is proposed by strain engineering [24–27]. The strain effect in graphene opens up a new direction in manipulating the electronic structure.

On the other hand, the band structure of graphene under a superlattice structure has attracted great interest [11–13,28–35]. It is theoretically reported that the electric superlattice could result in the strongly anisotropic renormalization of the carrier group velocity owing to their chiral nature, leading to the phenomenon of so-called supercollimation [28–30]. Extra Dirac points in the band structure corresponding to the zero averaged wave number have been experimentally observed [30–33]. On the contrary, in the magnetic superlattice, new finite-energy Dirac points are generated in the band structure and the Fermi velocity at zero-energy Dirac points is isotropically renormalized [11–13]. On the aspect of controlling transport property in graphene, the magnetic superlattice is more prominent due to Klein tunneling. However, the electric and magnetic superlattices alone cannot lift the valley degeneracy, and so works on the valley dependence of band structure are very few.

Experimentally, various proposals to engineer strain in graphene have been discussed [5,36,37]. A local strain can be achieved by patterning grooves, creases, steps, or wells in the substrate where graphene rests, so that different regions of the substrate interact differently with the graphene sheet, generating different strain profiles [7]. The strain can give rise to a pseudomagnetic field which preserves time-reversal symmetry, different from the real magnetic field. It is demonstrated that the graphene can sustain elastic strain up to 25% [38,39], paving an avenue for the development of strain-engineered electronics. The evidence for strain-induced spatial modulations in the local conductance of graphene on SiO_2 substrates has been already reported in experiment [40]. In addition, an inhomogeneous magnetic field on submicron scales in ordinary two-dimensional electron gases has been produced by ferromagnetic metal (FM) stripes [41,42] and superconducting materials [43]. A magnetic barrier with the strength up to 1 T and a length scale as low as 10 nm can be realized using nanolithography or domain walls [44]. It is believed that the same technologies can be used to create

*luweitao@lyu.edu.cn

similar magnetic fields in graphene [12]. The anomalous integer quantum Hall effect in graphene under a uniform magnetic field has been observed [10], which is caused by the $n = 0$ Landau level [45]. It is proved that the pseudomagnetic fields could interfere with the magnetic fields in many ways [46–49]. Recently, an unconventional splitting of Landau levels in strained graphene is observed due to the valley-polarized Landau level induced by the coexistence of the pseudomagnetic fields and magnetic fields [48].

Motivated by this literature, we consider a magnetic-strained superlattice in graphene, where the time-reversal symmetry is broken and the valley degeneracy is lifted. As a consequence, both energy band and transmission strongly depend on the valley feature. Different from the typical superlattices, the considered superlattice is composed of two different barriers (magnetic and strained barriers), providing more degrees of freedom when engineering the electrons, and so the unusual electronic structure is available. In particular, the miniband and band gap could be controlled independently. The valley-dependent band structure is reflected in transport property and provides a guide in enhancing the valley polarization.

The paper is organized as follows. In Sec. II we present the theoretical formalism and the dispersion relation. The numerical results on band structure and transmission for different valleys are shown in Secs. III and IV, respectively. Finally, we draw conclusions in Sec. V.

II. THEORETICAL MODEL

Let us consider a one-dimensional magnetic-strained superlattice in graphene formed by a series of magnetic barriers and strained barriers. Such a structure can be created by placing the graphene layer on a heterogeneous substrate with periodic steps and then depositing FM strips periodically on the top of graphene separated by a thin dielectric layer. Figure 1(a) shows a schematic illustration. The magnetization of the FM stripe is parallel to the graphene sheet, and so the electrons would feel a local magnetic field which can be expressed by $\mathbf{B}(x) = B\{z_0 a/(x^2 + z_0^2) - z_0 a/[(x-a)^2 + z_0^2]\}\hat{z}$, where $B = M_0 h/a$. M_0, h, and a are the magnetization, height, and width of strips, respectively, and z_0 is the distance between the strips and the graphene sheet. A local strain can be induced by a tension along the x direction applied on the structured substrate with a step [7], and the deformation can be described by a gauge vector potential $\mathbf{A}_S$ with opposite direction at the K and K' valleys. For the produced superlattice with smooth magnetic and strained barriers, the length scale of its spatial variation is much larger than the lattice constant of graphene, and the intervalley scattering is weak and can be neglected. In order to simplify the calculations and make the analysis clearer, the produced magnetic field may be well approximated as δ-function barriers $\mathbf{B}(x) = B[\delta(x) - \delta(x-a)]\hat{z}$. The corresponding vector potential in the Landau gauge is $\mathbf{A}_M(x) = Bl_B\Theta(x)\Theta(a-x)\hat{y}$, where l_B is the magnetic length and $\Theta(x)$ is the Heaviside step function. For simplicity, $\mathbf{A}_S$ is taken as $\mathbf{A}_S(x) = \delta t\,\Theta[x-(a+b)]\Theta[(a+b+c)-x]\hat{y}$, where δt is the strain-induced changes in the nearest-neighbor hopping amplitude t [6,7]. Therefore, the total effective vector potential fields for electrons near the K and K' valleys are

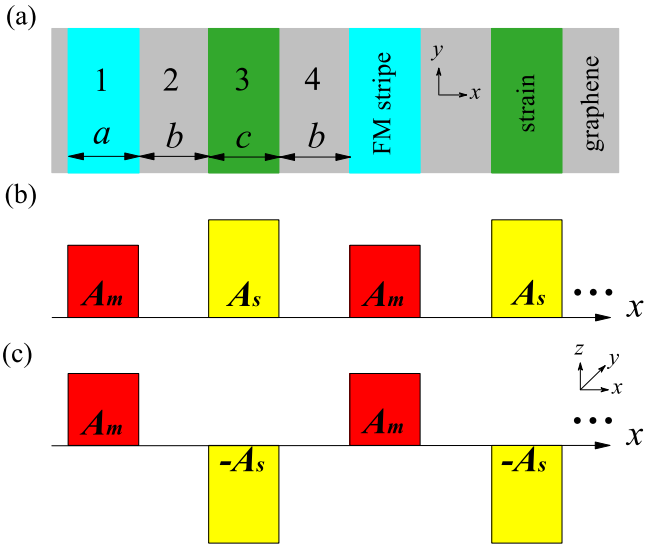

FIG. 1. (a) Schematic illustration of the magnetic-strained graphene superlattices produced by a series of FM stripes and substrate strains. (b) Theoretical model of the effective vector potential field for electrons in the K valley. (c) The same as that in (b) but for the K' valley. The length of one unit is $L = a + 2b + c$.

different, which could be theoretically modeled in Figs. 1(b) and 1(c), respectively. As a result, the valley degeneracy is expected to be lifted. Two units of such a structure are depicted in Fig. 1, and the length of one unit is $L = a + 2b + c$. We assume a short and wide magnetic-strained structure, i.e., its length in the x direction is much smaller than its width in the y direction, in which the edge effect could be neglected.

In the single-particle approximation, the electronic states at low energy could be described by the massless Dirac equation,

$$[v_F\sigma\cdot(\mathbf{p} + e\mathbf{A}_M + \xi e\mathbf{A}_S)]\Psi = E\Psi, \tag{1}$$

where v_F is the Fermi velocity, $\sigma = (\sigma_x, \sigma_y)$ is the Pauli matrix, and $\mathbf{p} = (p_x, p_y)$ is the momentum operator. $\xi = \pm 1$ corresponds to the K and K' valleys, respectively. The dimensionless units are introduced: $l_B = \sqrt{\hbar c/eB_0}$, $E_0 = \hbar v_F/l_B$, $B(x) \to B_0 B(x)$, $A_M(x) \to B_0 l_B A_M(x)$, $\vec{r} \to l_B\vec{r}$, $k \to k/l_B$, and $E \to E_0 E$. For $B_0 = 0.1T$, one has $l_B =$ 81 nm and $E_0 = 7$ meV. For a given incident energy E and transverse wave vector k_y, the eigenstate in the jth region has the form $\Psi_j(x,y) = \psi_j(x)e^{ik_y y}$ with

$$\psi_j(x) = G_j H_j \begin{pmatrix} a_j \\ b_j \end{pmatrix}, \tag{2}$$

where $G_j = \begin{pmatrix} 1 & 1 \\ (q_j + ik_j)/E & (-q_j + ik_j)/E \end{pmatrix}$, $H_j(x) = \begin{pmatrix} e^{iq_j x} & 0 \\ 0 & e^{-iq_j x} \end{pmatrix}$, $k_j = k_y + A_j$, q_j requires $q_j^2 + k_j^2 = E^2$, and A_j is A_M (or ξA_S) in the magnetic barriers (or strained barriers).

Based on the continuity condition of wave functions at the interface $x = x_j$ between the jth and $(j+1)$th regions, one can get $\binom{a_{j+1}}{b_{j+1}} = F_j\binom{a_j}{b_j}$, and $F_j = H_{j+1}^{-1}(x_j)G_{j+1}^{-1}G_j H_j(x_j)$. Thus, the total transfer matrix for the system with N regions can be written as $F = F_{N-1}\ldots F_j\ldots F_1$. Then the

transmission probability can be obtained from

$$T_{K,K'} = 1 - |F_{21}|^2/|F_{22}|^2, \tag{3}$$

and F_{ij} is the matrix element of F. The valley-dependent conductance at zero temperature can be written as

$$G_{K,K'}(E) = G_0 \int_{-\pi/2}^{\pi/2} T_{K,K'}(E, E\sin\theta)\cos\theta d\theta, \tag{4}$$

where θ is the incident angle with respect to the x direction, $G_0 = 2e^2 E L_y/(\pi\hbar)$ is taken as the conductance unit, and L_y is the sample size along the y direction. The valley polarization is defined as

$$P = (G_K - G_{K'})/(G_K + G_{K'}). \tag{5}$$

The dispersion relation can be also calculated by the transfer matrix method. Assuming $\binom{a_I}{b_I}$ and $\binom{a_F}{b_F}$ are the amplitudes of the wave functions before and after a unit, they could be related by transfer matrix:

$$\begin{pmatrix} a_F \\ b_F \end{pmatrix} = M \begin{pmatrix} a_I \\ b_I \end{pmatrix}, \tag{6}$$

where $M = H_2^{-1}(a+b+c)G_2^{-1}G_3H_3(a+b+c)H_3^{-1}(a+b)G_3^{-1}G_2H_2(a+b)H_2^{-1}(a)G_2^{-1}G_1H_1(a)G_1^{-1}G_2$. Based on the Bloch's theorem, the states in the superlattices satisfy

$$G_2H_2(x)\begin{pmatrix} a_F \\ b_F \end{pmatrix} = \exp(ik_xL)G_2H_2(x-L)\begin{pmatrix} a_I \\ b_I \end{pmatrix}, \tag{7}$$

and k_x is the Bloch wave number. Submitting Eq. (6) into Eq. (7) gives rise to

$$\det[H_2(L)M - \exp(ik_xL)] = 0. \tag{8}$$

The solution of Eq. (8) gives the dispersion relation $E(k_x)$ near the K and K' valleys, namely,

$$\cos(k_xL) = \cos(2q_2b)\cos(q_1a)\cos(q_3c) + \frac{k_y^2 + A_Mk_y - E^2}{q_2q_1}\sin(2q_2b)\sin(q_1a)\cos(q_3c) + \frac{k_y^2 + \xi A_Sk_y - E^2}{q_2q_3}\sin(2q_2b) \times \cos(q_1a)\sin(q_3c) + \frac{\xi A_MA_SE^2 - \left[q_2^4 - (A_M+\xi A_S)q_2^2k_y + \xi A_MA_Sk_y^2\right]\cos(2q_2b)}{q_2^2q_1q_3}\sin(q_1a)\sin(q_3c). \tag{9}$$

For K valley under a symmetric superlattice, that is, $A_M = A_S$ and $a = c$, the dispersion relation is governed a simpler transcendental equation,

$$\cos(k_xL) = \cos(q_1a)\cos(q_2b) - \frac{\left(q_1^2 + q_2^2 + A_M^2\right)}{2q_1q_2}\sin(q_1a)\sin(q_2b), \tag{10}$$

and $L = a + b$ here.

III. BAND STRUCTURE NEAR K AND K' VALLEYS

As seen from Eq. (9), the dispersion relation is invariant with respect to $k_x \to -k_x$ and $E \to -E$. The band structures near both K and K' valleys are symmetric with respect to $k_x = 0$ and the Fermi level. Thus, in what follows, we mainly focus on the conduction band. Since the electrons experience completely different superlattices near the K and K' valleys, the profound differences of electronic spectrum are expected.

A. Finite-energy Dirac points and group velocity

First, we discuss the band structures near the K and K' valleys under a symmetric superlattice. As shown in Figs. 2(a)– 2(c) for K valleys, the zero-energy Dirac point is shifted to $k_y = -1$ along $k_x = 0$, which satisfies $k_y = -A_M/2$, contrary to that observed in pristine graphene. The band curves are symmetric with respect to $k_y = -A_M/2$. Such a result is quite reasonable because the dispersion relation of Eq. (10) is invariant under the change $k_y \to -k_y - A_M$. It could be also understood based on the invariance of the effective potential $V_{\text{eff}}(k_y) = V_{\text{eff}}(-k_y - A_M)$, where $V_{\text{eff}} = (k_y + A_M + \xi A_S)^2$. As expected, finite-energy Dirac points are found along $k_y = -A_M/2$ [see Fig. 2(b)]. To find the locations of the Dirac points, we assume $k_x = 0, k_y = -A_M/2$, and $a = b = c$ in Eq. (10). Then Eq. (10) reduces to the form

$$\cos^2(qa) - \left(1 + \frac{A_M^2}{2q^2}\right)\sin^2(qa) = 1, \tag{11}$$

where $q^2 = q_{1,2}^2 = E^2 - (A_M/2)^2$. Equation (11) has the solutions for $1 + \frac{A_M^2}{2q^2} = -1$ or $\sin(qa) = 0$. The solution of

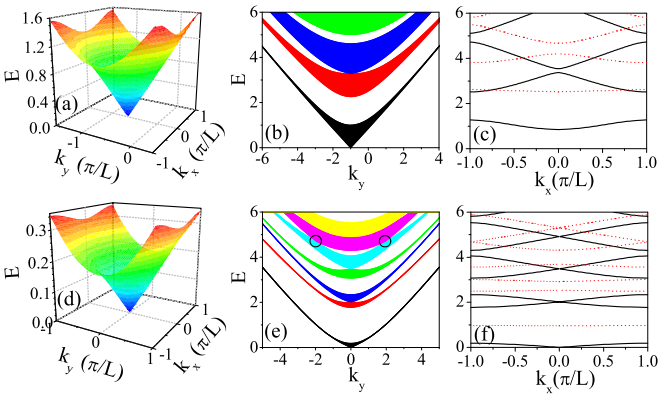

FIG. 2. Band dispersion near the (a–c) K and (d–f) K' valleys under the symmetric superlattices: (a,d) the lowest conduction miniband; (b,e) several low-energy minibands in (E,k_y) space; (c,f) energy spectrum vs k_x at $k_y = 0$ (solid curve) and 1.9 (dashed curve). The values of parameters are $A_M = A_S = 2$ and $a = b = c = 1$.

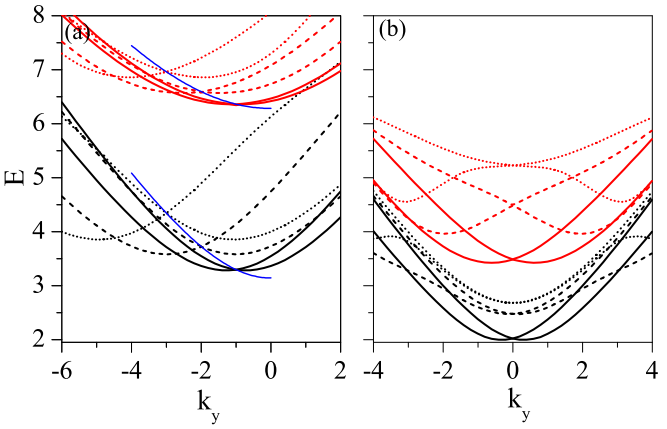

FIG. 3. The first (black curves) and the second (red curves) finite-energy Dirac points near (a) K and (b) K' valleys at $a = b = c = 1$. The solid, dashed, and dotted curves are for $A_M = A_S = 2$, 4, and 6, respectively.

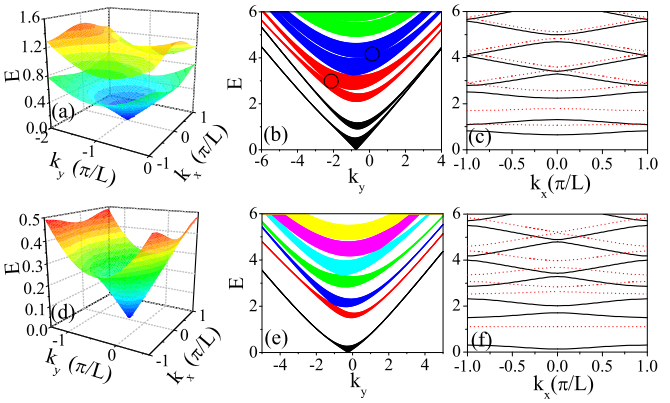

FIG. 4. Band dispersion near the (a–c) K and (d–f) K' valleys under the asymmetric superlattices: (a,d) the lowest conduction miniband; (b,e) several low-energy minibands in (E,k_y) space; (c,f) energy spectrum vs k_x at $k_y = 0$ (solid curve) and -2.1 (dashed curve). The values of parameters are $A_M = 2$, $A_S = 1$, and $a = b = c = 1$.

$1 + \frac{A_M^2}{2q^2} = -1$ is $E = 0$, corresponding to the zero-energy Dirac point. The solutions of $\sin(qa) = 0$ have the form

$$E_n = \pm\sqrt{\left(\frac{n\pi}{a}\right)^2 + \left(\frac{A_M}{2}\right)^2}, \tag{12}$$

corresponding to the finite-energy Dirac points, where n is the integer. Therefore, we could control the positions of the Dirac points in (E,k_y) space by adjusting the barrier height and barrier width. Figure 3(a) shows the variation of the first and the second finite-energy Dirac points with different barrier heights, and the blue lines are the curves on which the Dirac points are obtained by solving Eq. (12). The above result for the K valley is analogous to the general band spectrum with valley degeneracy discussed in the pure magnetic superlattices [11–13].

For the K' valley in Figs. 2(d)– 2(f), the Dirac points are located along $k_y = 0$, around which the energy spectrum is symmetric, due to the invariance of the dispersion relation of Eq. (9) under the change $k_y \to -k_y$. Contrary to the K valley, more finite-energy Dirac points appear in the considered energy region near the K' valley, by comparing Figs. 2(b) and 2(e). Assuming $k_x = k_y = 0$, $A_M = A_S$, and $a = b = c$, Eq. (9) for the K' valley can be rewritten as

$$\cos(2Ea)\cos^2(qa) - \frac{E}{q}\sin(2Ea)\sin(2qa) - \frac{A_M^2 + E^2\cos(2Ea)}{q^2}\sin^2(qa) = 1, \tag{13}$$

where $q^2 = E^2 - A_M^2$. Distinctly, $E = 0$ is one solution of Eq. (13), corresponding to the zero-energy Dirac point. The finite-energy Dirac points near the K' valley can be obtained by solving Eq. (13) numerically. It is clearly seen from Figs. 3(a) and 3(b) that the Dirac points near the K and K' valleys present alternative distribution in the energy region, which plays a basic role to the valley-dependent transport and the valley polarization, as discussed in Sec. IV. For both valleys, the widths of the minibands and the gaps strongly depend on E and k_y [see Figs. 2(b), 2(c), 2(e), and 2(f)]. As $|k_y|$ increases, the bands become narrower and independent of k_x. Consequently, the electrons are localized in the k_x direction and the motion becomes nearly unidimensional, indicating a collimation behavior along the k_y direction. Obviously, the collimation is more prominent in the K' valley. Furthermore, the circles in Fig. 2(e) manifest that there exist new level crossing points between the two minibands at the edges of the Brillouin zone ($k_x = \pm\pi/L$), implying the close of a band gap, which are also exhibited in Fig. 2(f) by the dashed curve. At the crossing point, the degeneracy of energy levels occurs when there is a Fabry-Pérot effect for the electron waves, achieving constructive interference in both the magnetic barrier and strained barrier. The crossing points emerge in pairs located symmetrically with respect to $k_y = 0$. Note that such crossing points are not found in the K valley under the symmetric superlattices.

Figure 4 shows the band structure for the (a–c) K and (d–f) K' valleys under a general asymmetric superlattice, that is, $A_M \neq A_S$ or $a \neq c$. For the K valley, the remarkable feature is that each degenerate miniband of the symmetric superlattices splits into two subminibands and produces a new band gap of the asymmetric superlattices [see Figs. 2(b) and 4(b)], due to a perturbation introduced by a different strained barrier of the complex unit. Interestingly, the subminibands become degenerate again at the edges of the Brillouin zone, forming crossing points (marked by the circles), which are clearly shown in Fig. 4(c). Opposite to the K valley, the minibands near the K' valley in Figs. 4(d)–4(f) stay degenerate. In addition, for both valleys, the zero-energy Dirac point is slightly shifted to $k_y = -(A_M + \xi A_S)/4$. However, it is more difficult to locate the finite-energy Dirac points which do not occur at $k_y = -(A_M + \xi A_S)/4$. The energy band is asymmetric with respect to $k_y = -(A_M + \xi A_S)/4$ [see Figs. 4(b) and 4(e)], contrary to the symmetric case, because the effective potential $V_{\text{eff}}(k_y)$ of the asymmetric superlattice is no longer invariant under the change $k_y \to -k_y - (A_M + \xi A_S)/2$. Note that a similar band structure could be also induced in the asymmetric superlattice by $a \neq c$. Furthermore, as the well width b

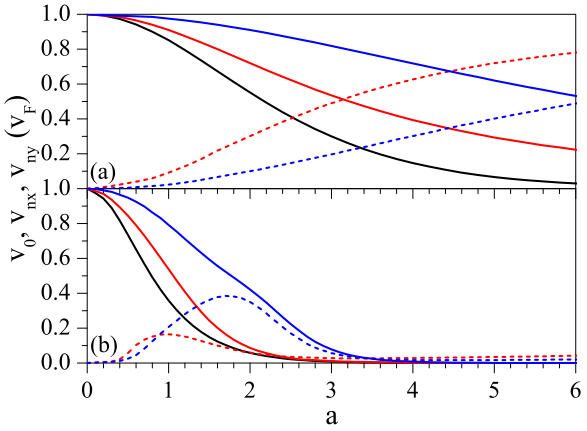

FIG. 5. Velocity vs barrier width for the (a) K and (b) K' valleys under the symmetric superlattices. The black solid curve is the group velocity v_0 at zero-energy Dirac point. The red solid, red dashed, blue solid, and blue dashed curves are the velocities v_{1x}, v_{1y}, v_{2x}, and v_{2y} at the first and the second finite-energy Dirac points, respectively. The parameters are set as $A_M = A_S = 2$ and $a = b = c$.

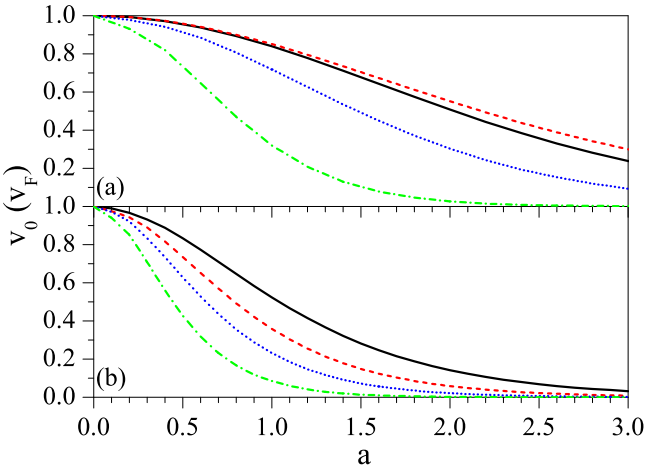

FIG. 6. Velocity v_0 vs barrier width for the (a) K and (b) K' valleys under the asymmetric superlattices at $A_M = 2$ and $a = b = c$. The solid, dashed, dotted, and dash-dotted curves are the velocity v_0 at zero-energy Dirac point at $A_S = 1$, 2, 3, and 5, respectively.

increases, more minibands would appear in the considered energy region for both valleys (not shown in the figure).

Now we turn to discuss the group velocities for the K and K' valleys, which are defined as $v_x/v_F = \partial E/\partial k_x$ and $v_y/v_F = \partial E/\partial k_y$. Figure 5 shows the velocities in units of v_F as a function of barrier width near the Dirac points for the (a) K and (b) K' valleys under the symmetric superlattices. For both valleys, the velocity at zero-energy Dirac point (black solid curve) is isotropic, whereas the velocities at finite-energy Dirac points (red and blue curves) are anisotropic. By expanding Eq. (10) at the zero-energy Dirac point ($E = 0$ and $k_y = -A_M/2$), the dispersion relation of the K valley could be obtained:

$$E = \pm \frac{A_M L/4}{\sinh(A_M L/4)} \sqrt{k_x^2 + (k_y + A_M/2)^2}, \qquad (14)$$

indicating an isotropic velocity. As the barrier width a increases, v_0 and the components v_{nx} ($n = 1,2$) decrease monotonically, because the electrons become more and more localized along the x direction by the magnetic-strained barrier. However, the variation of components v_{ny} is not monotonous. When the barrier width is relatively narrow ($a < 0.5$), $v_{nx} \to v_F$ while $v_{ny} \to 0$, suggesting a collimation along the k_x direction. By comparing Figs. 5(a) and 5(b) one may find that the velocity for the K valley is completely distinct from that for the K' valley, and the velocity for the K' valley is more sensitive to the change of barrier width. Dramatically, there exists a range of barrier width ($a > 3$) where the velocity for the K valley is finite, while the velocity for the K' valley is reduced almost to zero. Hence, we can achieve a normal conduction in the K valley and extremely low conduction in the K' valley simultaneously. This enables us to control the valley-dependent motion of electrons and realize valley polarization.

Figure 6 shows the velocity v_0 as a function of barrier width near the zero-energy Dirac point for the (a) K and (b) K' valleys under the general asymmetric superlattices for different values of A_S. We find that the asymmetry of superlattices does not destroy the isotropic dispersion near the zero-energy Dirac point and the anisotropic dispersion near finite-energy Dirac points for both valleys (not shown in the figure). The feature of the velocity in Fig. 6 is analogous to that discussed in Fig. 5. With the increase of strained barrier A_S, the velocity is suppressed gradually, and the renormalization for the K' valley is stronger.

Note that we mainly discussed the anisotropic dispersion induced by the superlattice. In graphene with a uniform uniaxial strain, the energy dispersion and the velocity also become anisotropic [50,51]. Actually, the strengths of magnetic and pseudomagnetic fields in the proposed system are a few tenths of a Tesla to a few Teslas. The pseudomagnetic field with such an order of magnitude could be produced by a very small strain, less than 1% [8], the effect of which on the velocity is very small, and the velocity is almost isotropic [6]. Therefore, we neglect the effect of the strain itself, compared with the superlattice-induced anisotropy. The above results demonstrate that electrons in the K and K' valleys have different band structures and group velocities, which can be used to realize valley polarization and construct a valley filter in graphene. Compared with the typical magnetic superlattices or strained superlattices, the magnetic-strained superlattices with a complex unit are more superior in controlling the band structure, as discussed in the following part.

B. Tunable miniband and band gap

In this part, we demonstrate that it is possible to manipulate the band structures and alter the position of the miniband independently by adjusting the strained barrier. Figure 7 presents the energy band in (E,k_y) space for (b, c) K and (d, e) K' valleys with different values of c, at $A_M = 2$, $A_S = 4$, and $a = b = 1$. In the absence of strain, i.e., $c = 0$, the band structures near the K and K' valleys are the same [see Fig. 7(a)] and the valley electrons are degenerate, leading to identical transmission and zero polarization. In the presence of strain ($c \neq 0$), the valley degeneracy is lifted. With the increase of c, it is found that for the K valley the second miniband shifts

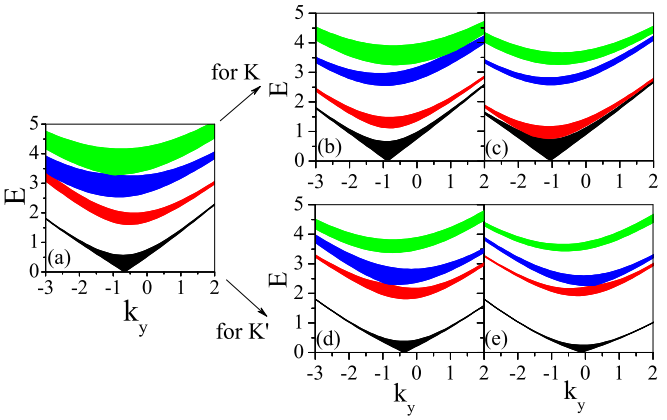

FIG. 7. Energy band in (E,k_y) space for the (b, c) K and (d, e) K' valleys at $A_M = 2$, $A_S = 4$, and $a = b = 1$, $c = 0$ in (a), 0.2 in (b, d), and 0.4 in (c, e).

down gradually and finally combines with the first miniband [see Figs. 7(b) and 7(c)]. Oppositely, for the K' valley the second miniband shifts up to the third miniband and the band gap between them becomes smaller [see Figs. 7(d) and 7(e)]. Simultaneously, the zero-energy Dirac point moves to the left (or right) along k_y for the K (or K') valley and the finite-energy Dirac points are shifted as well. However, it should be noted that other minibands are insensitive to the change of c. Such a behavior could be understood as follows. In fact, the strong and narrow strain could be regarded as a perturbation of the pure magnetic superlattices, which is set in the potential well. The strain works as a barrier (or well) for the K (or K') valley, which mainly affects the bound state of the second miniband and leads to a shift of the miniband.

Figure 8 shows the dependence of the miniband and the band gap on the strain width c for the (a) K and (b) K' valleys. For the K valley in Fig. 8(a), the second and the first minibands move closer and merge with each other at $c \approx 0.45$ where the band gap is closed. For the K' valley in Fig. 8(b), the second and the third minibands merge with each other at $c \approx 0.25$. As a consequence, the width of the merged miniband is enlarged. Interestingly, the widths of the minibands keep almost constant

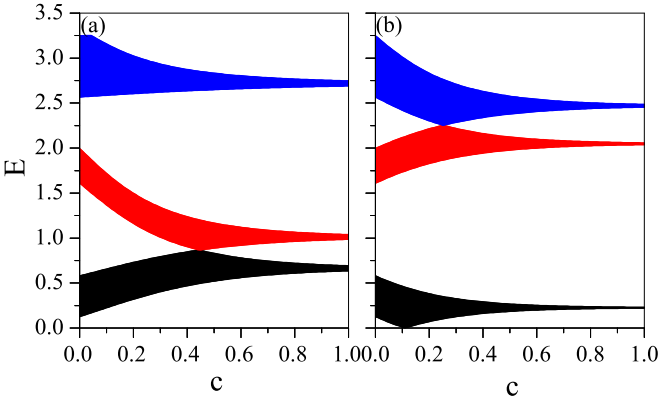

FIG. 8. Three lowest energy minibands vs the width c of the strain for the (a) K and (b) K' valleys at $A_M = 2$, $A_S = 4$, $a = b = 1$, and $k_y = -0.5$.

before merging. With the further increase of c, the widths begin to become narrow, and the closed band gap is reopened. At the same time, the positions of other minibands weakly depend on the width c, such as the third miniband for the K valley and the first miniband for the K' valley. Therefore, the band gap between the merged miniband and its adjacent miniband is enlarged by adjusting c. Indeed, other minibands could be also controlled by properly adjusting the position of strain in the potential well. An analogous technique for engineering the bands of two-dimensional electron gas by electric superlattices was discussed in previous literature [52]. The ability to control the miniband and band-gap widths independently is of a great value for tuning of the tunneling current and electro-optic switches [52,53], and it also offers possible application in infrared photodetectors, in which it is desirable to have only two minibands with a small band gap [54].

In fact, the properties of the band structure under the magnetic-strained superlattices could be generalized to a pure magnetic superlattice with the same spatial structure (such as symmetric, antisymmetric, or asymmetric), but the valleys are degenerate. The characteristics of graphene mainly depend on the electrons near the K and K' valleys. Therefore, our discussion on the band structure for the K and K' valleys should be helpful in manipulating the electronic structure and could be used to understand and control the valley-dependent transport, as discussed in the following.

IV. VALLEY-DEPENDENT TRANSPORT

In this section we discuss the properties of valley-dependent transport through a finite magnetic-strained superlattice and their relation with band structure. The superiority of the considered system is reflected in controlling the valley-dependent transmission. Note that in the absence of strain, the transmission is independent of the valleys, because the valley degeneracy cannot be lifted by the magnetic field alone due to the inversion symmetry of the graphene lattice [55]. In the absence of the magnetic field, the transmissions at the K and K' valleys present just mirror symmetry with respect to $k_y = 0$, because the strain-induced pseudomagnetic fields are of opposite directions at the K and K' valleys and do not break the time-reversal symmetry. Accordingly, the strain or the magnetic field alone cannot generate a valley-polarized current in graphene. However, a combination of the magnetic field and the strain could lift the valley degeneracy and break the time-reversal symmetry, leading to valley polarization.

Figure 9 shows the transmission in (E,k_y) space for (a, b) K and (c, d) K' valleys, under the (a, c) symmetric and (b, d) asymmetric superlattices, taking the period number $n = 2$ as example. The dashed curves indicate the borders for different electronic states inside the potential wells. One can clearly see that for both valleys, the transmissions are restricted in the region $-E < k_y < E$ where the states inside the potential wells are traveling waves. For the K valley in Fig. 9(a), the distribution of transmission is asymmetric, although the band structure is symmetric around $k_y = -(A_M + A_S)/4$ [see Fig. 2(b)]. The resonant regions composed of many peaks become narrow and move to the high-energy region as k_y increases. Under the asymmetric superlattices, the resonant regions present split [see Fig. 9(b)]. For the K' valley in

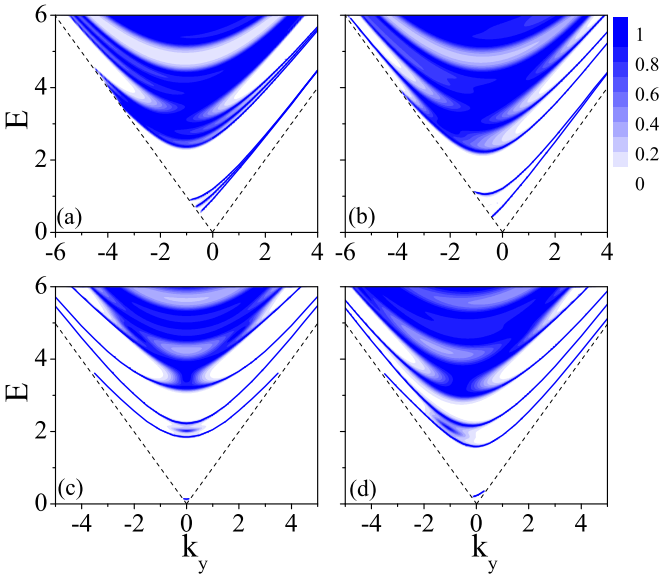

FIG. 9. Contour plot of the transmission $T_{K,K'}(E,k_y)$ for the (a, b) K and (c, d) K' valleys at $A_M = 2$, $a = b = c = 1$, and $n = 2$. (a, c) The symmetric case with $A_S = 2$ and (b, d) the asymmetric case with $A_S = 1$.

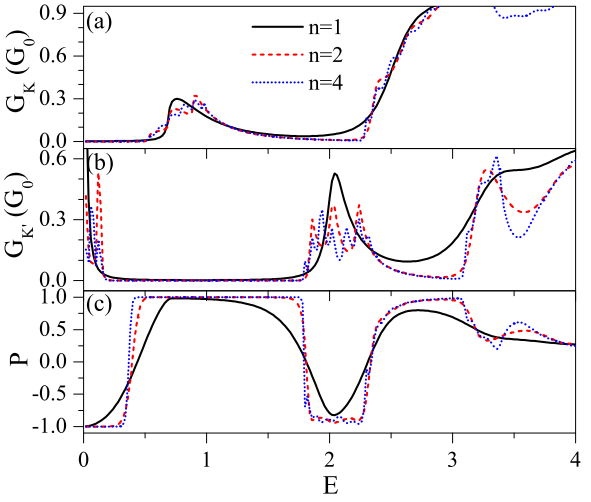

FIG. 10. Conductance $G_{K,K'}$ vs Fermi energy for the (a) K and (b) K' valleys and (c) the polarization P at $A_M = A_S = 2$ and $a = b = c = 1$.

Fig. 9(c), the transmission is symmetric around $k_y = 0$, which is destroyed by the asymmetric superlattices [see Fig. 9(d)]. The resonant characteristic of transmission arises from a combined effect of the resonant states in the wells and the barriers, which are more pronounced in the low-energy region. Comparison with Figs. 2 and 4 indicates that the distribution of transmission spectra is completely consistent with the band structure, that is, the resonant transmission (or transmission gap) corresponds to the miniband (or band gap). Furthermore, one may find that the transmission probability $T_{K,K'}$ is always equal to unity at the positions of the Dirac points and the crossing points, which manifest themselves in the transmission. Such a robust feature results from the Fabry-Pérot interference effect of the incident electron inside the potential barrier. At these particular points, the Fabry-Pérot resonances with $T_{K,K'} = 1$ could occur in transmission with constructive interference, different from the Klein paradox. Figure 9 reveals the strong valley-dependent feature of transmission, and the resonances exist in different energy regions for electrons in the K and K' valleys.

The valley-dependent transmission feature is reflected in the conductance. Figure 10 displays the conductance for the (a) K and (b) K' valleys and (c) the corresponding valley polarization as a function of Fermi energy with different periods n. As n increases, the positions of the resonant conductances for both valleys are invariant, and the conductance in the nonresonant region is suppressed gradually [see Figs. 10(a) and 10(b)]. Because the degenerate energy levels in the potential wells become nondegenerate and split due to the tunnel effect, the resonant peak of the conductance presents a split. In the low-energy region ($E < A_M$ or A_S), the resonance is mainly contributed by the resonant modes in the wells. When the incident energy is higher than the barriers, it provides new propagating modes; as a result, the resonance becomes indistinct and the conductance increases rapidly. Significantly, the conductances G_K and $G_{K'}$ present alternative distribution in the energy region, i.e., G_K nearly vanishes for those energies where $G_{K'}$ is in resonance and vice versa. These features can be understood based on the band structure in Figs. 2 and 3 and the transmission probability in Fig. 9. The resonant conductance (or conductance gap) corresponds to the miniband (or band gap). It is worth noting that the Dirac points appear as pronounced peaks in the conductance. This result directly leads to a remarkable valley polarization, as shown in Fig. 10(c). The polarization oscillates with Fermi energy in a decayed way. The polarization can reach 100% when $E < A_M$, and disappears gradually when $E > A_M$ due to the small difference between G_K and $G_{K'}$. Furthermore, the polarization is greatly enhanced by increasing n, indicating that a relatively large period is beneficial to the valley polarization. In addition, the polarization could be controlled by virtue of the finite-size effect. The increase of barrier width a or c would enhance the polarization. As the well width b increases, more resonant modes and more resonant conductances would appear in the considered energy region, resulting in more perfect polarization platforms (not shown in the figure).

Figure 11 shows the effect of the strain strength and the Fermi energy on valley polarization in the (a) symmetric and (b) asymmetric cases. For both cases in the absence of strain $A_S = 0$, the valley degeneracy is not lifted and so the polarization vanishes, although A_M breaks the time-reversal symmetry in the asymmetric cases. With the presence and the increase of A_S, the polarization increases gradually and reaches 100%. The perfect polarization at a given Fermi energy can be achieved by adjusting the strain strength. Obviously, the polarization exhibits a controllable switching effect with Fermi energy. Comparison between Figs. 11(a) and 11(b) indicates that the polarization is insensitive to the symmetry of the system's structure.

We have discussed the controllability of the minibands and the band gaps for the K and K' valleys in Figs. 7 and 8, and it is beneficial to tune the valley-dependent conductance, as

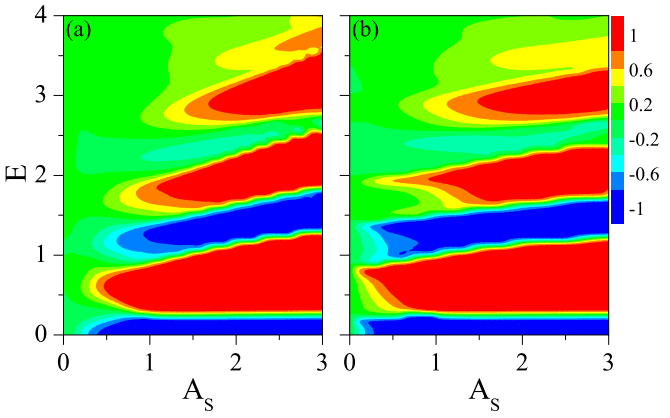

FIG. 11. Contour plot of the valley polarization $P(E, A_S)$ at $a = c = 1$, $b = 2$, and $n = 2$. (a) The symmetric case with $A_M = A_S$ and (b) the asymmetric case with $A_M = 2$.

demonstrated in Fig. 12. Figure 12 shows the conductances (a) G_K, (b) $G_{K'}$, and (c) the polarization P as a function of Fermi energy with different widths c. As c increases, the second resonance moves to the low (or high) energy region and merges with the first (or the third) resonance for the K (or K') valley, while other resonances are almost constant. Furthermore, the corresponding resonant conductance and conductance gap are enlarged. Such a feature arises from the band structure in Fig. 7. As a consequence, the perfect polarization is broadened in the energy region [see Fig. 12(c)].

The perfect polarization mainly occurs in the low-energy region in the above results. In fact, the polarization region could be also controlled by the external voltages. The local electric field U induced by the voltage is assumed to be finite in the strained and magnetic barrier regions and zero otherwise. An electron at low energy could be approximately described by the Dirac equation

$$[v_F \sigma \cdot (\mathbf{p} + e\mathbf{A}_M + \xi e\mathbf{A}_S) + U\hat{I}]\Psi = E\Psi, \qquad (15)$$

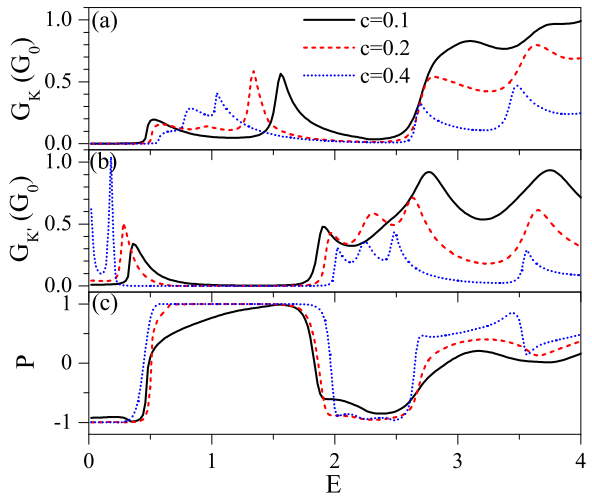

FIG. 12. Conductance $G_{K,K'}$ vs Fermi energy for the (a) K and (b) K' valleys and (c) the polarization P at $A_M = 2$, $A_S = 4$, $a = b = 1$, and $n = 2$.

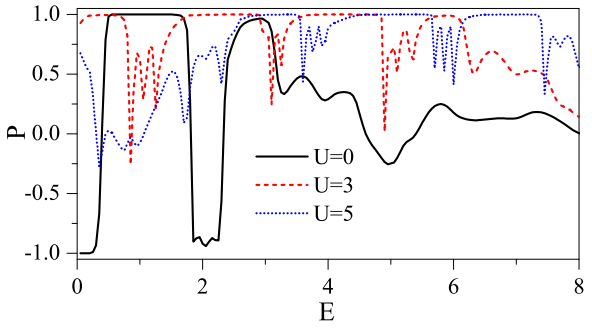

FIG. 13. Polarization P vs Fermi energy at $A_M = A_S = 2$, $a = b = c = 1$, and $n = 2$.

and $\hat{I}$ is a 2×2 unit matrix. In the presence of U, the conduction and valence minibands shift to the higher-energy region, and the minibands for the K' valley become narrower compared to the K valley. As a result, the transmission resonances for both valleys shift to the higher-energy region, and the conductance $G_{K'}$ strongly decreases while G_K stays finite. The electrons around the K valley give a dominant contribution to the conductance. Therefore, the perfect polarization shifts to the higher-energy region and the minimum $P = -1$ disappears gradually as U increases, as seen from Fig. 13.

In the above discussions, we take an ideal structure in Figs. 1(b) and 1(c) to illustrate the operating principles of the proposed system. However, it does not hamper its significance to a realistic system, because the basic electronic properties do not depend on the actual shape of the superlattices but depend on its structure. Figure 14 discusses the conductance and polarization through a realistic system shown in the inset. The realistic profile of a magnetic field produced by the ferromagnetic stripe is $\mathbf{B}(x) = B\{z_0 a/(x^2 + z_0^2) - z_0 a/[(x-a)^2 + z_0^2]\}\hat{z}$, and the corresponding magnetic vector potential has the form $\mathbf{A}_M(x) = Ba[\tan^{-1}(\frac{x}{z_0}) - \tan^{-1}(\frac{x-a}{z_0})]\hat{y}$. We use a smooth profile to model a realistic gauge potential produced

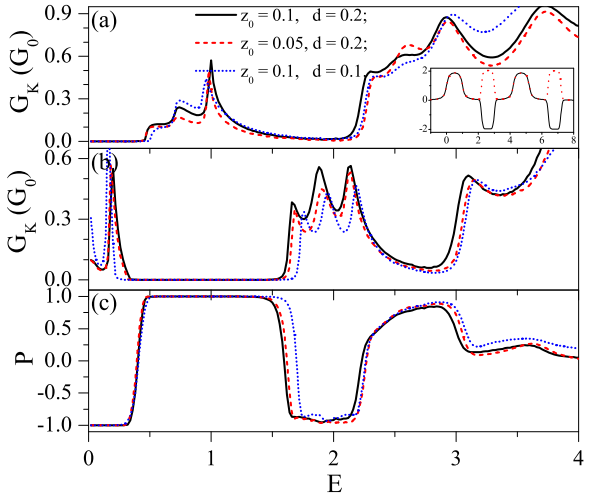

FIG. 14. Conductance $G_{K,K'}$ vs Fermi energy for the (a) K and (b) K' valleys and (c) the polarization P through the realistic system at $B = 0.7$, $A_0 = 2.0$, $a = b = c = 1.0$, and $n = 2$. The solid and dashed curves in the inset of (a) are the realistic vector potentials for electrons near the K' and K valleys, respectively.

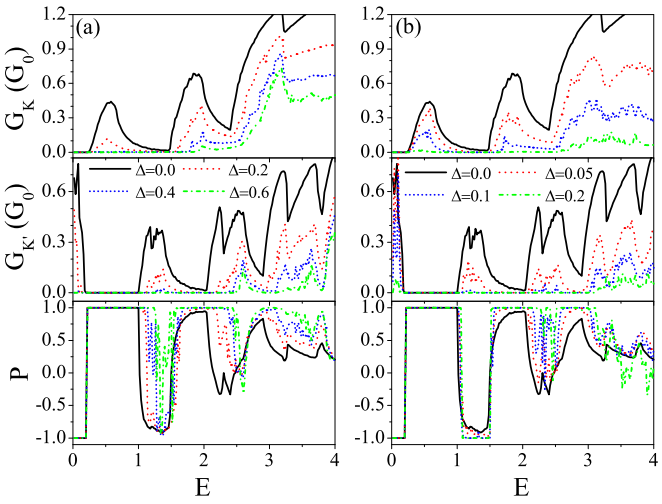

FIG. 15. Conductance $G_{K,K'}$ and polarization P vs Fermi energy when (a) the barrier heights and (b) barrier/well widths present disorder, and $n = 50$. $A_{M0} = A_{S0} = 1.5$, $b = 2.0$, and $a = c = 1.0$ in (a). $A_M = A_S = 1.5$, $b_0 = 2.0$, and $a_0 = c_0 = 1.0$ in (b).

by the substrate strain, $\mathbf{A}_S(x) = \frac{A_0}{2}[\mathrm{erf}(\frac{2[x-(a+b)]}{d} - 2) + \mathrm{erf}(\frac{2[(a+b+c)-x]}{d} - 2)]\hat{y}$, where $\mathrm{erf}(x)$ is the error function, A_0 is the amplitude, and d determines the width of the crossover region [25]. Therefore, the total profile of the relatively realistic vector potential $\mathbf{A}_M + \xi\mathbf{A}_S$ is obtained (see the inset of Fig. 14). Figure 14 displays that the conductances G_K and $G_{K'}$ present alternative distribution in the energy region, leading to a remarkable valley polarization analogous to that observed in an ideal model. For the realistic system, with decreasing z_0 and d, the profiles of vector potentials A_M and A_S become gradually sharper, respectively, which tend to the ideal case. The results in Fig. 14 suggest that the transmission is insensitive to the profiles of the structure. The realistic system could be also used as a valley filter.

Due to the random nature of the experimental techniques, the disorder of the barrier in superlattices is unavoidable. In Fig. 15 we discuss the effect of disorder on the conductance and valley polarization. We set disorder situations in which the values of barrier heights $A_{M,S}$ fluctuate around their mean values, given by $\langle A_{M,S}\rangle = A_{M0,S0}$. The fluctuations are given by $A_{M,S}|_i = A_{M0,S0}(1 + \Delta\eta_i)$, where $\{\eta_i\}$ is a set of uncorrelated random variables or white noise, $-1 < \eta_i < 1$, Δ is the disorder strength, and i is the site index. In the same manner, the disorder of the barrier and well widths can be given by $(a,b,c)|_i = (a_0,b_0,c_0)(1 + \Delta\eta_i)$. Figure 15(a) shows the effect of the disorder of barrier heights. With the presence and increase of the disorder strength Δ, the conductances for both valleys are suppressed, but the positions of resonant conductances are nearly invariable, leading to the excellent polarization. Notably, the disorder enhances the valley polarization compared with the order case. As shown in Fig. 15(b), the effect of the disorder of barrier and well widths on the transmission is similar to that observed in Fig. 15(a), but the disorder effect of widths is more prominent. The results provide evidence that the disorder has no fundamental influence on the valley-dependent transmission, because the superlattices for electrons near the K and K' valleys are qualitatively different and the disorder just induces a quantitative change on the superlattices.

V. CONCLUSION

In summary, we studied the valley-dependent band structure and transport property of graphene under a periodic magnetic-strained field, where the valley degeneracy is lifted and the time-reversal symmetry is broken. The electrons near the K and K' valleys are dominated by different effective superlattices, and so they possess a strong valley-dependent feature, leading to some peculiar properties which are not found in magnetic superlattice [11–13] and strain superlattice [34,35], such as the valley dependence of the minibands, Dirac points, Fermi velocity, and transmission; the ability of controlling the miniband and band gap independently; and the valley filtering effect. The main findings are as follows:

(1) Under the symmetric superlattices, the energy bands for both valleys are symmetric with respect to $k_y = -(A_M + \xi A_S)/4$, at which the Dirac points are located. Dirac points near the K and K' valleys present alternative distribution in the energy region. More finite-energy Dirac points, more prominent collimation behavior, and new crossing points at the edges of the Brillouin zone are found for the K' valley. The degenerate miniband near the K valley splits into two subminibands and produces a new band gap under the asymmetric superlattices.

(2) For both valleys, the velocities at zero (finite) energy Dirac points are isotropically (anisotropically) renormalized, which are robust against the symmetry of the superlattices. However, the velocity for the K' valley is greatly renormalized compared with the K valley, and we can achieve a finite velocity for the K valley while the velocity for the K' valley is zero.

(3) It is possible to manipulate the position of the miniband independently by appropriately adjusting the strained barrier. The widths of the miniband and the band gap can be enlarged or reduced, which is beneficial to tune the conductance and broaden the polarization platform.

(4) The transmission spectrum is consistent with the band structure, and the transmission presents strong valley-dependent feature. The Dirac points appear as pronounced peaks in conductance. The electrons in opposite valleys can be perfectly transmitted or totally reflected. Therefore, a remarkable valley polarization is achieved which can be controlled by the strain, the period, and the voltage. The high polarization, which is insensitive to the disorder, still holds in the realistic system.

The main results, including band structure and transport property, are robust against the changes of structural parameters. The proposed system may provide a reference for controlling the electronic structure of other two-dimensional Dirac materials. Finally, we hope these results can be helpful for understanding the electronic property near the valleys and benefit potential applications of the valley filter device.

ACKNOWLEDGMENT

This work was supported by the NSFC (11404157).

[1] A. Gupta, T. Sakthivel, and S. Seal, Prog. Mater. Sci. **73**, 44 (2015).

[2] K. S. Novoselov, A. K. Geim, S. V. Morozov, D. Jiang, Y. Zhang, S. V. Dubonos, I. V. Grigorieva, and A. A. Firsov, Science **306**, 666 (2004).

[3] Y. W. Son, M. L. Cohen, and S. G. Louie, Phys. Rev. Lett. **97**, 216803 (2006).

[4] M. Y. Han, B. Özyilmaz, Y. Zhang, and P. Kim, Phys. Rev. Lett. **98**, 206805 (2007).

[5] X. Li, X. Wang, L. Zhang, S. Lee, and H. Dai, Science **319**, 1229 (2008).

[6] V. M. Pereira, A. H. Castro Neto, and N. M. R. Peres, Phys. Rev. B **80**, 045401 (2009).

[7] V. M. Pereira and A. H. Castro Neto, Phys. Rev. Lett. **103**, 046801 (2009).

[8] F. Guinea, M. I. Katsnelson, and A. K. Geim, Nat. Phys. **6**, 30 (2010).

[9] D. B. Zhang, G. Seifert, and K. Chang, Phys. Rev. Lett. **112**, 096805 (2014).

[10] Y. Zhang, Y. Tan, H. L. Stormer, and P. Kim, Nature (London) **438**, 201 (2005).

[11] L. Z. Tan, C. H. Park, and S. G. Louie, Phys. Rev. B **81**, 195426 (2010).

[12] L. Dell'Anna and A. De Martino, Phys. Rev. B **83**, 155449 (2011).

[13] V. Q. Le, C. H. Pham, and V. L. Nguyen, J. Phys.: Condens. Matter **24**, 345502 (2012).

[14] A. Rycerz, J. Tworzydło, and C. W. J. Beenakker, Nat. Phys. **3**, 172 (2007).

[15] A. R. Akhmerov, J. H. Bardarson, A. Rycerz, and C. W. J. Beenakker, Phys. Rev. B **77**, 205416 (2008).

[16] J. L. Garcia-Pomar, A. Cortijo, and M. Nieto-Vesperinas, Phys. Rev. Lett. **100**, 236801 (2008).

[17] J. M. Pereira, Jr., F. M. Peeters, R. N. C. Filho, and G. A. Farias, J. Phys.: Condens. Matter **21**, 045301 (2009).

[18] D. Gunlycke and C. T. White, Phys. Rev. Lett. **106**, 136806 (2011).

[19] D. Gunlycke, S. Vasudevan, and C. T. White, Nano Lett. **13**, 259 (2013).

[20] L. Xiao-Ling, L. Zhe, Y. Hai-Bo, J. Li-Wei, G. Wen-Zhu, and Z. Yi-Song, Phys. Rev. B **86**, 045410 (2012).

[21] Y. Liu, J. T. Song, Y. X. Li, Y. Liu, and Q. F. Sun, Phys. Rev. B **87**, 195445 (2013).

[22] D. R. da Costa, A. Chaves, S. H. R. Sena, G. A. Farias, and F. M. Peeters, Phys. Rev. B **92**, 045417 (2015).

[23] M. Vozmediano, M. Katsnelson, and F. Guinea, Phys. Rep. **496**, 109 (2010).

[24] Z. Wu, F. Zhai, F. M. Peeters, H. Q. Xu, and K. Chang, Phys. Rev. Lett. **106**, 176802 (2011).

[25] F. Zhai, X. Zhao, K. Chang, and H. Q. Xu, Phys. Rev. B **82**, 115442 (2010).

[26] Y. Jiang, T. Low, K. Chang, M. I. Katsnelson, and F. Guinea, Phys. Rev. Lett. **110**, 046601 (2013).

[27] M. M. Grujić, M. Ž. Tadić, and F. M. Peeters, Phys. Rev. Lett. **113**, 046601 (2014).

[28] M. Barbier, P. Vasilopoulos, and F. M. Peeters, Phys. Rev. B **81**, 075438 (2010).

[29] C. H. Park, Y. W. Son, L. Yang, M. L. Cohen, and S. G. Louie, Nano Lett. **8**, 2920 (2008).

[30] C. H. Park, L. Yang, Y. W. Son, M. L. Cohen, and S. G. Louie, Nat. Phys. **4**, 213 (2008).

[31] L. Brey and H. A. Fertig, Phys. Rev. Lett. **103**, 046809 (2009).

[32] L. G. Wang and S. Y. Zhu, Phys. Rev. B **81**, 205444 (2010).

[33] M. Yankowitz, J. Xue, D. Cormode, J. D. Sanchez-Yamagishi, K. Watanabe, T. Taniguchi, P. Jarillo-Herrero, P. Jacquod, and B. J. LeRoy, Nat. Phys. **8**, 382 (2012).

[34] S. Gattenlöhner, W. Belzig, and M. Titov, Phys. Rev. B **82**, 155417 (2010).

[35] F. M. D. Pellegrino, G. G. N. Angilella, and R. Pucci, Phys. Rev. B **85**, 195409 (2012).

[36] T. Low and F. Guinea, Nano Lett. **10**, 3551 (2010).

[37] J. Lu, A. C. Castro Neto, and K. P. Loh, Nat. Commun. **3**, 823 (2012).

[38] C. Lee, X. Wei, J. W. Kysar, and J. Hone, Science **321**, 385 (2008).

[39] K. S. Kim, Y. Zhao, H. Jang, S. Y. Lee, J. M. Kim, K. S. Kim, J. H. Ahn, P. Kim, J. Y. Choi, and B. H. Hong, Nature (London) **457**, 706 (2009).

[40] M. L. Teague, A. P. Lai, J. Velasco, C. R. Hughes, A. D. Beyer, M. W. Bockrath, C. N. Lau, and N.-C. Yeh, Nano Lett. **9**, 2542 (2009).

[41] A. Nogaret, D. N. Lawton, D. K. Maude, J. C. Portal, and M. Henini, Phys. Rev. B **67**, 165317 (2003).

[42] A. Tarasov, S. Hugger, H. Xu, M. Cerchez, T. Heinzel, I. V. Zozoulenko, U. Gasser-Szerer, D. Reuter, and A. D. Wieck, Phys. Rev. Lett. **104**, 186801 (2010).

[43] H. A. Carmona, A. K. Geim, A. Nogaret, P. C. Main, T. J. Foster, M. Henini, S. P. Beaumont, and M. G. Blamire, Phys. Rev. Lett. **74**, 3009 (1995).

[44] A. Nogaret, J. Phys.: Condens. Matter **22**, 253201 (2010).

[45] V. P. Gusynin and S. G. Sharapov, Phys. Rev. Lett. **95**, 146801 (2005).

[46] E. Prada, P. San-Jose, G. León, M. M. Fogler, and F. Guinea, Phys. Rev. B **81**, 161402(R) (2010).

[47] B. Roy, Z. X. Hu, and K. Yang, Phys. Rev. B **87**, 121408(R) (2013).

[48] S. Y. Li, K. K. Bai, L. J. Yin, J. B. Qiao, W. X. Wang, and L. He, Phys. Rev. B **92**, 245302 (2015).

[49] D. O. Rybalka, E. V. Gorbar, and V. P. Gusynin, Phys. Rev. B **91**, 115132 (2015).

[50] H. Rostami and R. Asgari, Phys. Rev. B **86**, 155435 (2012).

[51] K. Nakatsuji, T. Yoshimura, F. Komori, K. Morita, and S. Tanaka, Phys. Rev. B **85**, 195416 (2012).

[52] P. Vasilopoulos, F. M. Peeters, and D. Aitelhabti, Phys. Rev. B **41**, 10021 (1990).

[53] H. Schneider, K. Kawashima, and K. Fujiwara, Phys. Rev. B **44**, 5943 (1991).

[54] K. K. Choi, B. F. Levine, C. G. Bethea, J. Walker, and R. J. Malik, Phys. Rev. Lett. **59**, 2459 (1987).

[55] However, an external magnetic field can lift the valley degeneracy of graphene by virtue of electron-electron or electron-phonon interactions [Phys. Rev. Lett. **96**, 136806 (2006); Nature (London) **462**, 192 (2009); Nat. Phys. **8**, 550 (2012)]. Opposite to graphene, the inversion symmetry is naturally broken in transition metal dichalcogenides, providing a more applicable paradigm for the magnetic-field-induced valley Zeeman effect [**11**, 148 (2015); **11**, 141 (2015); Phys. Rev. B **91**, 075433 (2015)].